

# The ZIMPOL high contrast imaging polarimeter for SPHERE: polarimetric high contrast commissioning results

Ronald Roelfsema<sup>\*a</sup>, Andreas Bazzon<sup>b</sup>, Hans Martin Schmid<sup>b</sup>, Johan Pragt<sup>a</sup>, Alain Govaert<sup>a</sup>, Daniel Gisler<sup>b</sup>, Carsten Dominik<sup>c</sup>, Andrea Baruffolo<sup>d</sup>, Jean-Luc Beuzit<sup>e</sup>, Anne Costille<sup>g</sup>, Kjetil Dohlen<sup>g</sup>, Mark Downing<sup>f</sup>, Eddy Elswijk<sup>a</sup>, Menno de Haan<sup>a</sup>, Norbert Hubin<sup>f</sup>, Markus Kasper<sup>f</sup>, Christoph Keller<sup>h</sup>, Jean-Louis Lizon<sup>f</sup>, David Mouillet<sup>e</sup>, Alexey Pavlov<sup>i</sup>, Pascal Puget<sup>e</sup>, Bernardo Salasnich<sup>d</sup>, Jean-Francois Sauvage<sup>j</sup>, Francois Wildi<sup>k</sup>

a) NOVA Optical-Infrared Instrumentation Group at ASTRON, Oude Hoogeveensedijk 4, 7991 PD Dwingeloo, The Netherlands; b) Institute of Astronomy, ETH Zurich, 8093 Zurich, Switzerland; c) Astronomical Institute “Anton Pannekoek”, 1098 SJ Amsterdam, The Netherlands; d) INAF, Osservatorio Astronomico di Padova, 35122 Padova, Italy; e) IPAG, Université Joseph Fourier, BP 53, 38041 Grenoble cedex 9, France; f) ESO, Karl-Schwarzschild-Strasse 2, D-85748 Garching bei München, Germany; g) LAM, UMR6110, CNRS/Universite de Provence, 13388 Marseille cedex 13, France; h) Leiden Observatory, Niels Bohrweg 2, P.O. Box 9513, 2300 RA Leiden, The Netherlands; i) Max-Planck-Institut für Astronomie, Königstuhl 17, 69117 Heidelberg, Germany; j) ONERA, BP 72, 92322 Chatillon France; k) Observatoire Astronomique de l’Université de Geneve, 1290 Sauverny, Switzerland;

## Abstract

SPHERE (Spectro-Polarimetric High-contrast Exoplanet Research) is a second generation VLT instrument aimed at the direct detection of exo-planets. It has received its first light in May 2014. ZIMPOL (Zurich Imaging Polarimeter) is the imaging polarimeter subsystem of the SPHERE instrument. It's capable of both high accuracy and high sensitivity polarimetry but can also be used as a classical imager. It is located behind an extreme AO system and a stellar coronagraph. ZIMPOL operates at visible wavelengths which is best suited to detect the very faint reflected and hence polarized visible light from extra solar planets. During the SPHERE fourth commissioning period (October 2014) we have made deep coronagraphic observations of the bright star alpha Gru ( $m_R = 1.75$ ) to assess the high contrast polarimetric performance of SPHERE-ZIMPOL. We have integrated on the target for a total time of about 45 minutes during the meridian transit in the Very Broad Band filter (600 - 900 nm) with a classical Lyot coronagraph with  $3 \lambda/D$  radius focal mask. We reduce the data by a combination of Polarized Background subtraction, Polarimetric Differential Imaging (PDI) and Angular Differential Imaging (ADI). We reach contrasts of  $10^{-6}$  and  $10^{-7}$  at a radial distances of respectively 7 and 14  $\lambda/D$  from the PSF core. At these radial distances we are respectively a factor of 10 and 2 above the photon noise limit. We discuss our results by considering the temporal and spatial speckle behavior close to the PSF core in combination with low order polarimetric aberrations.

**Keywords:** SPHERE, ZIMPOL, High Contrast Imaging, Polarimetric, Extreme Adaptive Optics, Coronagraph, VLT

## 1. INTRODUCTION

SPHERE-ZIMPOL<sup>[1][2][3][4][5][6][7]</sup> (Spectro-Polarimetric High Contrast Exoplanet Research - Zurich Imaging Polarimeter) is one of the first instruments which aim for the direct detection of reflected light from extra-solar planets. The instrument will search for direct light from old planets with orbital periods of a few months to a few years as we know them from our solar system. These are planets which are in or close to the habitable zone.

The reflected radiation is generally polarized<sup>[8][9]</sup> and the degree of polarization may be particularly high at short wavelengths  $< 1 \mu\text{m}$  due to Rayleigh scattering by molecules and scattering by haze particles in planetary atmospheres. For this reason the visual-red spectral region is well suited for planet polarimetry.

There are half a dozen of good candidate systems for which giant planets should be detectable, even if their properties are not ideal (low albedo, not highly polarized). In another handful targets there is some chance to find high-polarization planets, if they exist around them. For stars further away a detection of reflected light with SPHERE-ZIMPOL will be difficult.

\*roelfsema@astron.nl; phone +31-(0)521-595 172; www.astron.nl

The basic ZIMPOL principle for high-precision polarization measurements includes a fast liquid crystal polarization modulator (FLC) with a modulation frequency in the kHz range, combined with a CCD detector which demodulates the intensity signal in synchronism with the polarization modulation<sup>[10][11][12]</sup>. The modulation frequency is much faster than the seeing variations and therefore ZIMPOL is able to capture two subsequent images with nearly identical turbulent phase screens. We refer to the FLC switching as Single Difference Polarization.

By rotating a half-wave plate (HWP2) far upstream in the optical path by 45°, the sign of the incoming Stokes Q polarization is reversed<sup>[13]</sup>. The instrumental aberrations, on the other hand, remain unchanged, resulting in the same background landscape as before. If the polarization images before and after the signal switching are subtracted from one another, the real polarization signals of the astronomical target add up constructively while the static background is canceled out. We refer to the HWP2 switching as Double Difference Polarization.

### 1.1 Observational conditions

In the context of the high contrast performance assessment of SPHERE-ZIMPOL we have made deep coronagraphic observations of the bright star alpha Gru ( $m_R = 1.75$ ). During the SPHERE fourth commissioning period (9 October 2014) we have integrated on the target for a total time of about 45 minutes during the meridian transit in the Very Broad Band (VBB) filter. We have used the ZIMPOL P1 mode in the FastPolarimetry detector read-out mode in combination with a classical Lyot coronagraph with  $3 \lambda/D$  radius focal mask.

We have observed in moderate atmospheric conditions for Paranal standards. The seeing, windspeed and coherence time during the run are shown in Figure 1. The median seeing was about 0.85 arcsec and the median windspeed around 8 m/sec. Our observations span about 45 minutes. Unfortunately the atmospheric conditions worsened in the course of time as can be seen from Figure 1.

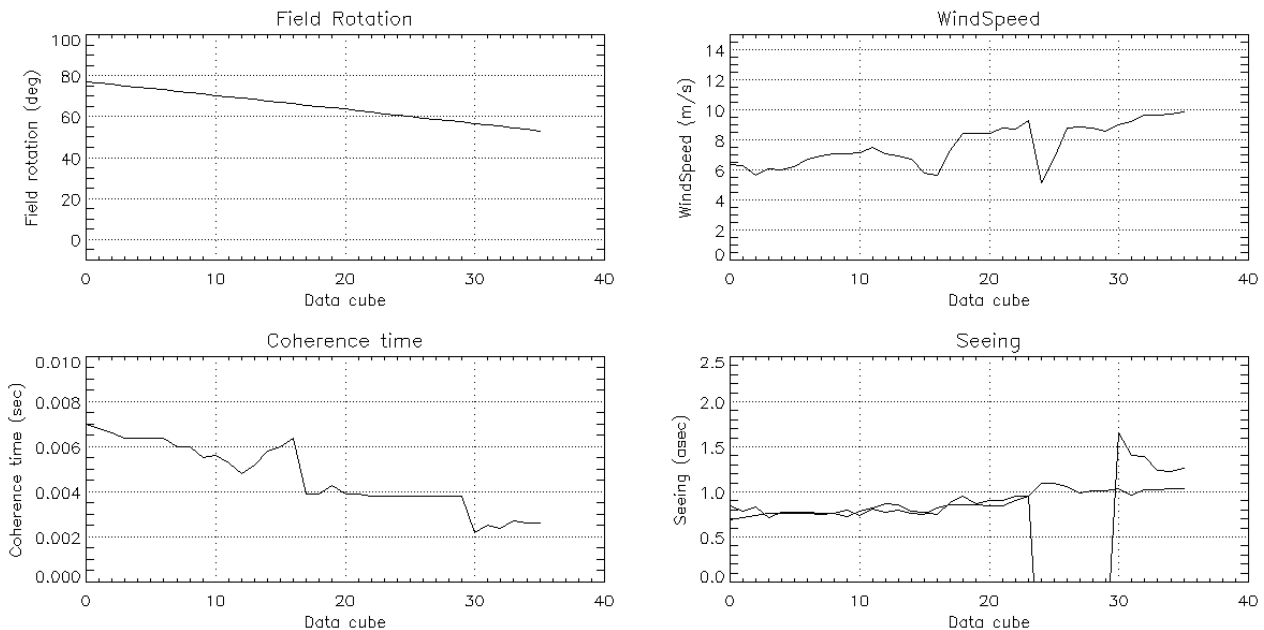


Figure 1 Observational conditions as retrieved from the fits headers. Field rotation (top left), wind speed (top right), correlation time  $\tau_0$  (bottom left) and seeing (bottom right). The data cube number is indicated on the horizontal axis, i.e. each data cube is about 1 minute.

## 1.2 Data reduction

The ZIMPOL observation is divided in four datasets corresponding to the two FLC states (UP and DOWN) and the two HWP2 states (00 and 45). Therefore, we have the following datasets:

```
DATA_00_UP
DATA_00_DN
DATA_45_UP
DATA_45_DN
```

In the next step we use these datasets to construct two Single Difference (SD) frames according to

```
SD00 = DATA_00_UP - DATA_00_DN
SD45 = DATA_45_UP - DATA_45_DN
```

And finally we use the SD frames to construct the Double Difference (DD) frame:

```
DD = (SD45 - SD00)/2
```

We have acquired a total of 1800 frames with a DIT of 1.1 sec. The HWP2 has been switched in a QU-cycle after every 50 frames.

## 2. INTENSITY

### 2.1 Non-Coronagraphic and Coronagraphic intensity profiles

The PSF non-coronagraphic and coronagraphic profiles are shown in Figure 2. The PSF peak of the non-coronagraphic profile is used for the contrast estimates as described later. Also shown in Figure 2 are the azimuthal averaged intensity profiles. The profiles are normalized to the non-coronagraphic PSF peak intensity.

We see that the profiles are more or less overlapping beyond a radius of about 200 mas. Outside this radius the coronagraphic profile even seems a bit higher than the non-coronagraphic profile. We attribute this to the fact that the non-coronagraphic profile is recorded at the start of the observations with the best atmospheric conditions. Nevertheless, we can conclude that we have an intensity reduction better than a factor of 100 w.r.t. the PSF peak beyond a radius of 100 mas.

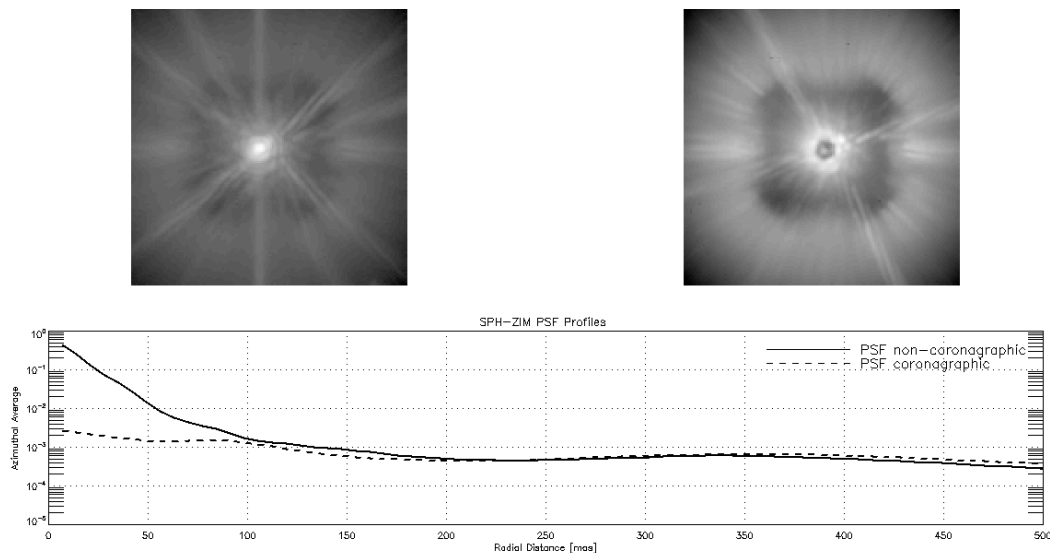


Figure 2 PSF Profiles. The top panel shown the non-coronagraphic PSF (left) and coronagraph profile (right). The bottom panel shows the azimuthal average profiles normalized to the non-coronagraphic PSF peak intensity.

## 2.2 Speckle statistics

To assess the noise in the raw data we have considered the speckle statistics. As illustration we show the time traces of the DATA\_00\_UP dataset of four selected speckles (see Figure 3):

- A. Focal Mask Edge - 60 mas
- B. Bright speckle - 120 mas
- C. Dark region middle - 248 mas
- D. Dark region close to control radius - 318 mas

The time traces are represented as histograms in Figure 4. Especially for the brighter speckles we observe a skewed profile that is well described by a modified Rician-distribution<sup>[14]</sup>, i.e. a relatively small random phasor that exists on top of a constant phasor:

$$p(I) = \frac{1}{I_s} \exp\left(-\frac{I+I_c}{I_s}\right) I_0\left(\frac{2\sqrt{I}\sqrt{I_c}}{I_s}\right)$$

where  $I_0$  is the zero-order modified Bessel function of the first kind,  $I_c$  indicates the constant phasor and  $I_s$  the random phasor, i.e. we associate  $I_c$  to the static speckle and  $I_s$  to the random speckle. We have fitted the distributions to find the values of  $I_c$  and  $I_s$ . The fits are over plotted in red traces on top of the experimental data in black. In general we see that the experimental data can be very well described with the modified Rician distribution.

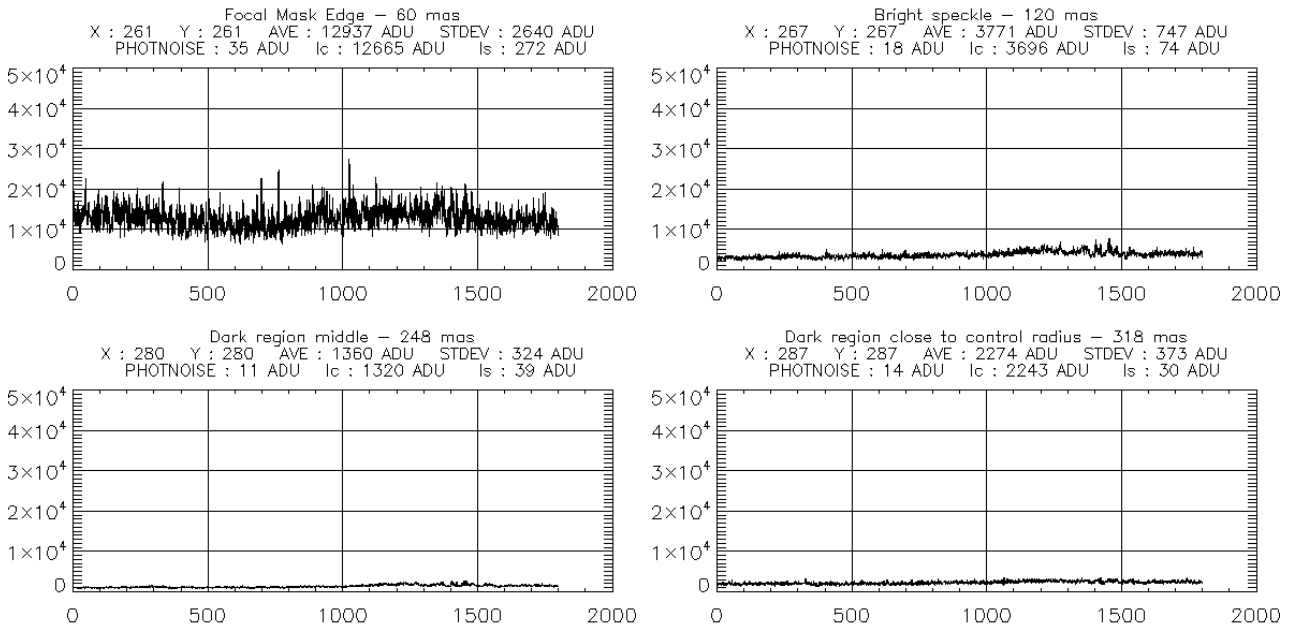


Figure 3 Time traces of four selected speckles.

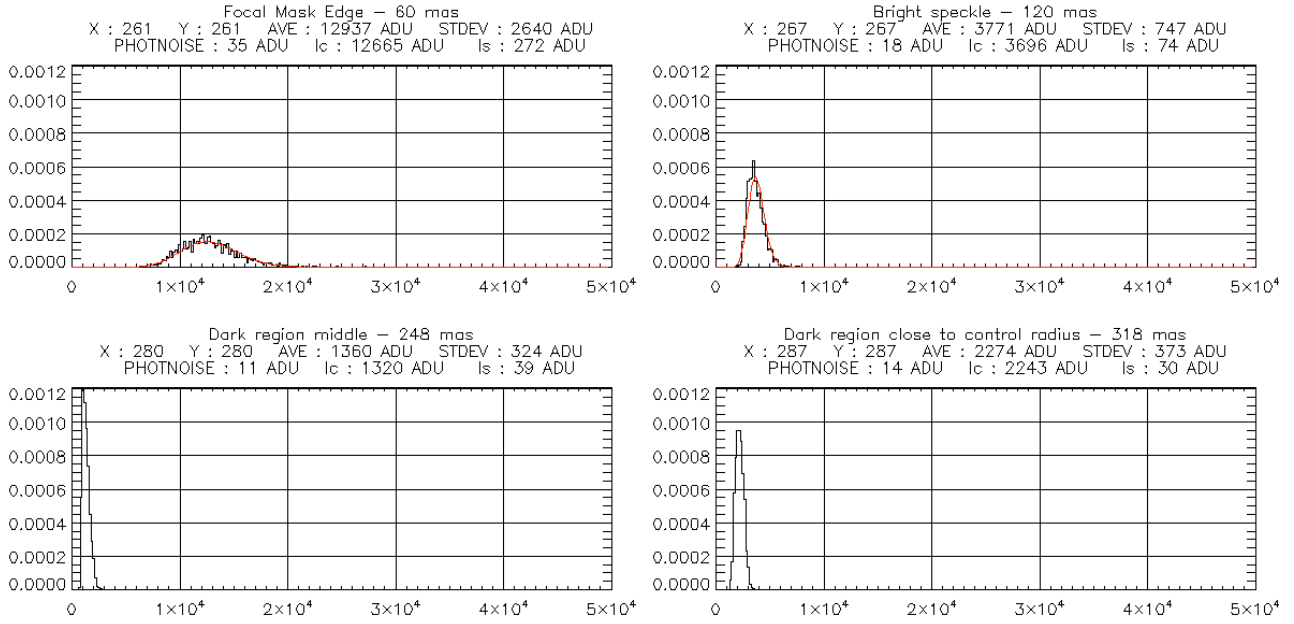


Figure 4 Histograms of measured intensity of four selected speckles (black) with over plotted fit of modified Rician distribution (red).

Of particular interest is the expression for the variance of the distribution:

$$\sigma^2 = I_s^2 + 2I_s I_c + I_c + I_s$$

The terms on the left hand side from left to right are: the random speckle  $I_s^2$ , a cross-term  $2I_s I_c$  between the static and the random phasor, i.e. the random speckle is amplified by the static speckle and the photon noise  $I_c + I_s$ . Figure 5 shows the azimuthal average of each term. It's evident that the cross-term is dominating the random noise behavior over the other two terms. Therefore we approximate the overall noise level as

$$\sigma = \sqrt{2I_s I_c}$$

We see from this expression that the static speckle has a major impact on the random noise. Therefore, we conclude that simplified assumptions that the static speckle can be calibrated by subtraction are not valid. A map of the static speckle  $I_c$  and random speckle  $I_s$  is shown in Figure 6.

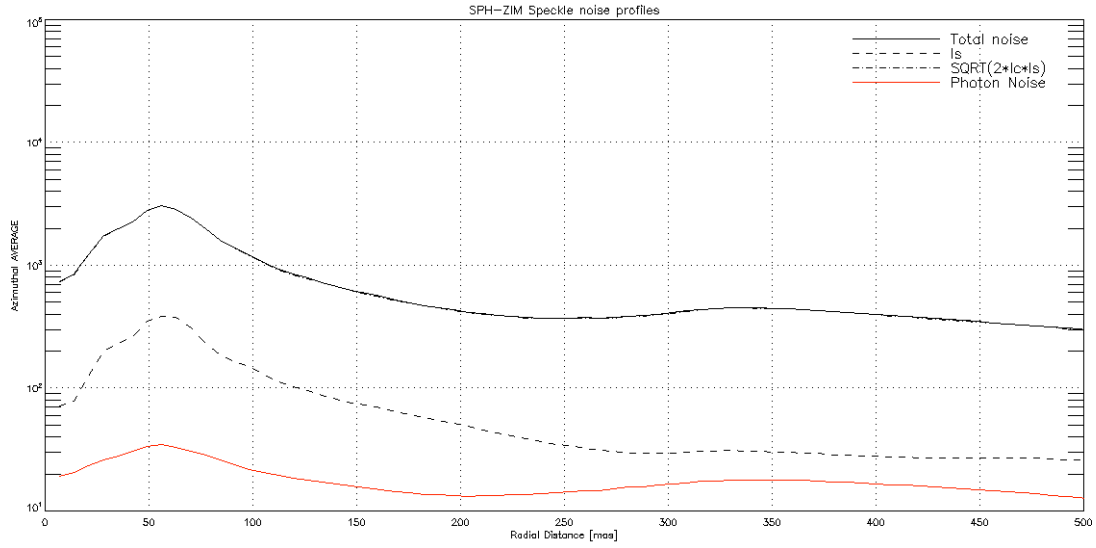


Figure 5 Speckle noise profiles. Azimuthal average profiles of the three terms in the speckle standard deviation as measured in the image, random noise  $I_s$ , cross term  $\text{SQRT}(2I_c I_s)$  and the Photon Noise  $\text{SQRT}(I_c + I_s)$ . The individual noise terms are added quadratically to obtain the Total Noise. In this plot the cross term is almost on top of the Total Noise, i.e. the cross term is the dominating noise contribution.

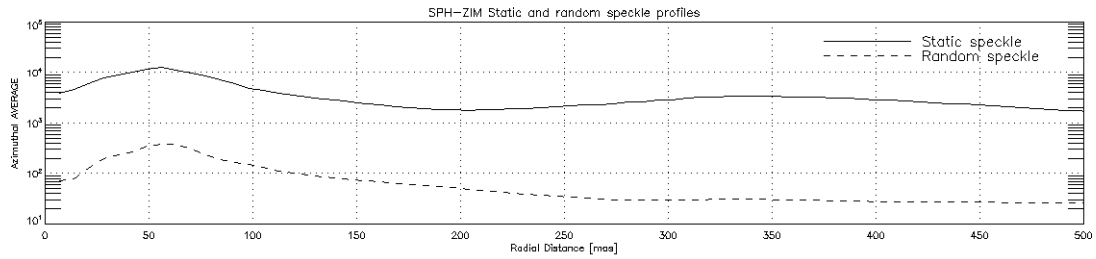
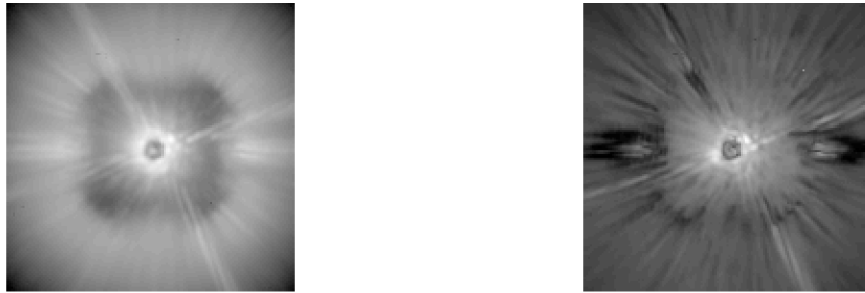


Figure 6 Static and random speckle profiles. (top panel) Static speckle  $I_c$  (left) and random speckle  $I_s$  (right). (bottom panel) Azimuthal average profiles of static and random speckle.

### 3. POLARIZATION

#### 3.1 Single Difference polarization

The purpose of the ZIMPOL Single Difference is to provide a very fast sampling of the random speckle in order to achieve temporal correlations. Figure 7 illustrates this with a zoom of the sampling of the DATA\_00\_UP and DATA\_00\_DN traces. The close but not perfect resembles of both traces is evident from the plots.

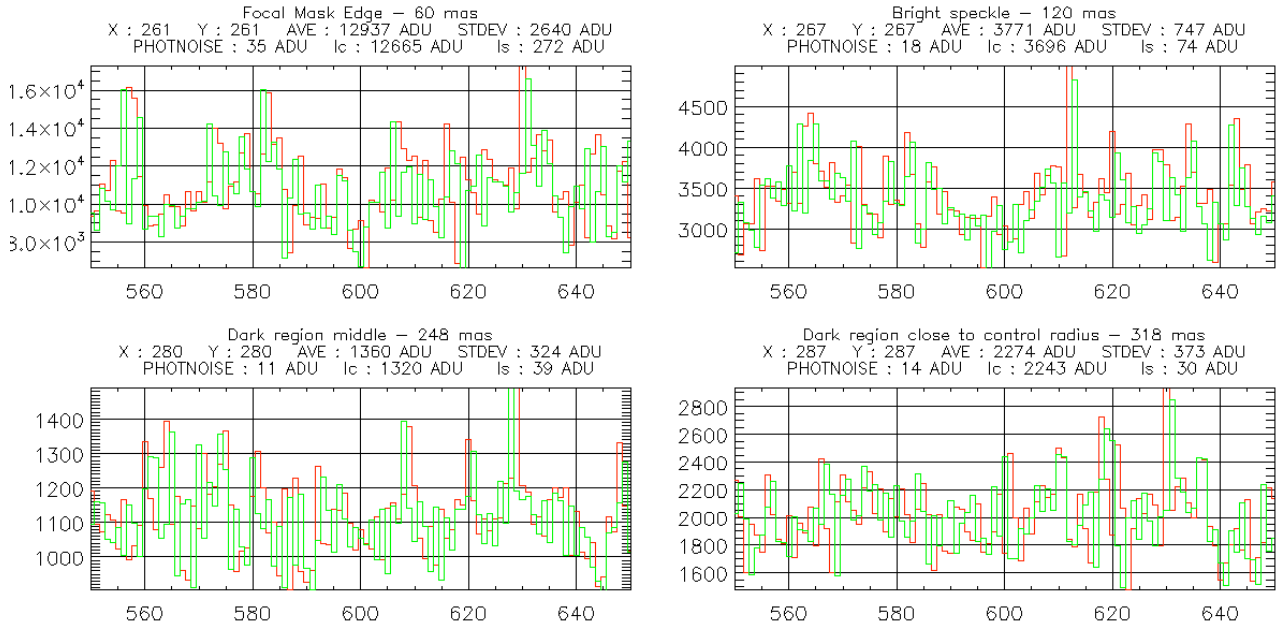


Figure 7 Single Difference time traces for four selected speckles. DATA\_00\_UP is shown in red and DATA\_45\_DN is shown in green. The two datasets sample the speckle pattern quasi synchronous with a time difference of 0.5 msec, i.e. much faster than the random speckle life time.

The correlation of the traces can be quantified with the covariance, i.e. the noise in the SD00 frame is given by

$$Var(SD00) = Var(DAT_00_UP) + Var(DATA_00_DN) - 2Cov(DATA_00_UP, DATA_00_DN)$$

In this relation the variances  $Var(DATA_00_UP)$  and  $Var(DATA_00_DN)$  are determined by speckle noise. The covariance  $Cov(DATA_00_UP, DATA_45_DN)$  is related to FLC effects that cause non-perfect synchronous speckle sampling: ratio FLC switch time/speckle lifetime, ratio FLC switch time/transient transition time, FLC – Detector synchronization.

We use N frames to determine the error in the mean value of the individual datasets. For our alpha Gru observations we have obtained

HWP2_00	18 datacubes of 50 frames
HWP2_45	18 datacubes of 50 frames

then  $N = 18 * 50 = 900$  frames. The error in the mean for DATA\_00\_UP for instance is then given by

$$\sigma_{00\_UP} = \frac{\sigma}{\sqrt{N}}$$

where  $\sigma$  is the standard deviation of the dataset. Similar expressions are valid for the other datasets. We combine the datasets to find the following expressions for the noise in the Single Difference datasets:

$$\sigma_{SD00}^2 = \frac{1}{N} [\sigma_{00\_UP}^2 + \sigma_{00\_DN}^2 - 2Cov(00\_UP, 00\_DN)]$$

$$\sigma_{SD45}^2 = \frac{1}{N} [\sigma_{45\_UP}^2 + \sigma_{45\_DN}^2 - 2Cov(45\_UP, 45\_DN)]$$

If we assume

$$\sigma^2 = \sigma_{00\_UP}^2 = \sigma_{00\_DN}^2 = \sigma_{45\_UP}^2 = \sigma_{45\_DN}^2$$

and use

$$r_{SD} = Cov/\sigma^2$$

where Cov is the Covariance and  $r_{SD}$  is the Correlation Coefficient for the Single Difference signal, then we can write

$$\sigma_{SD} = \sigma \sqrt{\frac{2}{N} (1 - r_{SD})}$$

as we have seen earlier according to Rician statistics  $\sigma$  can be approximated as

$$\sigma = \sqrt{2I_C I_S}$$

The values of the correlation coefficient will be in the range from -1 to 1 where a value of 1 indicates perfect correlation, a value of 0 indicates uncorrelated signals and a value of -1 indicates anti-correlated signals.

Figure 8 shows a map and azimuthal profiles of the SD correlation coefficient. We observe a typical correlation of about 0.80 in the center of the control radius around 150 mas. The correlation is even increasing further outward to about 0.87 around 200 mas and then decreasing again towards the AO control radius. However, we see a decrease in correlation towards the PSF core dropping to about 0.5 at the edge of the coronagraph focal mask.

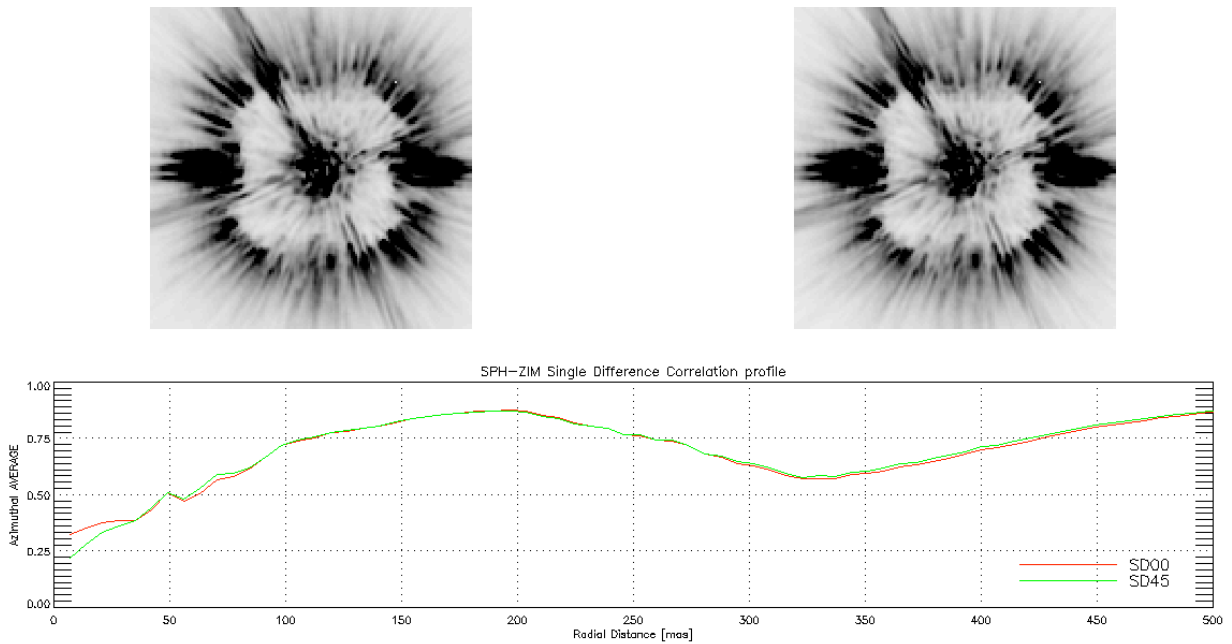


Figure 8 Single Difference: Correlation profiles. (top panel) Map of correlation coefficient of SD00 (left) and SD45 (right). (bottom panel) Azimuthal average profiles of SD00 and SD45 correlation coefficients. We observe a very close match between the two SD profiles.

### 3.2 Double Difference polarization

The purpose of the Double Difference is threefold:

1. Temporal switch to calibrate the quasi-static speckle
2. Subtract the polarized background of the instrument
3. Calibrate the FLC differential aberrations

In this section we will address these three items.

Similar as for the Single Difference we can write for the noise in the Double Difference:

$$\sigma_{DD}^2 = \frac{1}{2} \sqrt{2\sigma_{SD}^2 - 2\sigma_{SD}^2 r_{DD}} = \frac{1}{\sqrt{2}} \sigma_{SD} \sqrt{1 - r_{DD}}$$

$$r_{DD} = \sigma \sqrt{\frac{(1-r_{SD})(1-r_{DD})}{N}}$$

where  $r_{DD}$  is the Correlation Coefficient for the Double Difference signal

#### Temporal switch

Time traces for the SD00 (red) and SD45 (green) are shown in Figure 9. Also the time trace for the DD (blue) is indicated. In general we observe that the time traces consist of the sum of two random traces with different time scale: a rapidly changing noise term attributed to the temporal rapid variations of the atmosphere and a slowly varying random time trend attributed to the quasi static speckle. The slowly varying trend is over plotted with the solid traces in Figure 9. The fast switching FLC is supposed to beat the rapidly changing random speckle whereas the HWP2 is supposed to switch on time scales faster than the typical time scale of the quasi-static speckle.

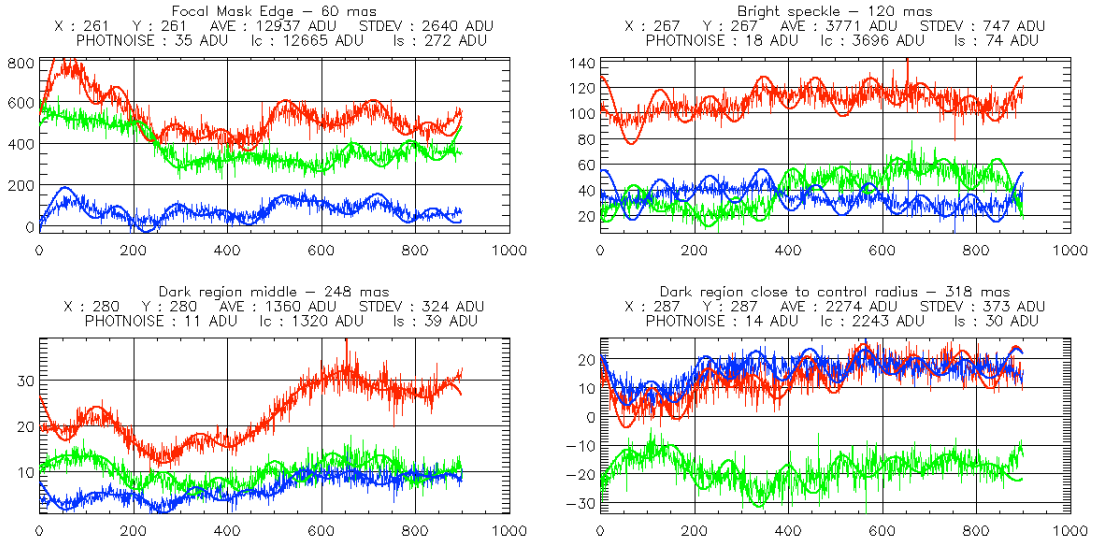


Figure 9 Double Difference: Time traces for four selected speckle with SD00 in red, SD45 in green and DD in blue.

The two SD traces are not recorded simultaneously. Therefore, to study the cross correlation between the two SD traces we first consider the auto correlation of the quasi-static part of the individual SD traces.

Figure 10 shows the autocorrelation of the quasi-static part for the SD00 traces. For our observations we have switched after 50 frames and we can see from the curves that the correlation after 50 frames is already very low. We have made a simple curve fit to the auto correlation curves that is only valid in the auto correlation coefficient range between 0.6 and 1.0. We fit a simple curve  $r = 1 - a*t^2$  to the experimental data.

To achieve a significant noise reduction of about a factor 2 to 3 we need an auto correlation better than 0.7. We calculate from the fit the correlation time that is needed for  $a > 0.7$ . The results are shown in Figure 11. We conclude that we need that we need to switch HWP2 about every 20 seconds to achieve a performance increase of a factor of 2 and faster than about every 5 seconds for a performance increase of a factor of 5.

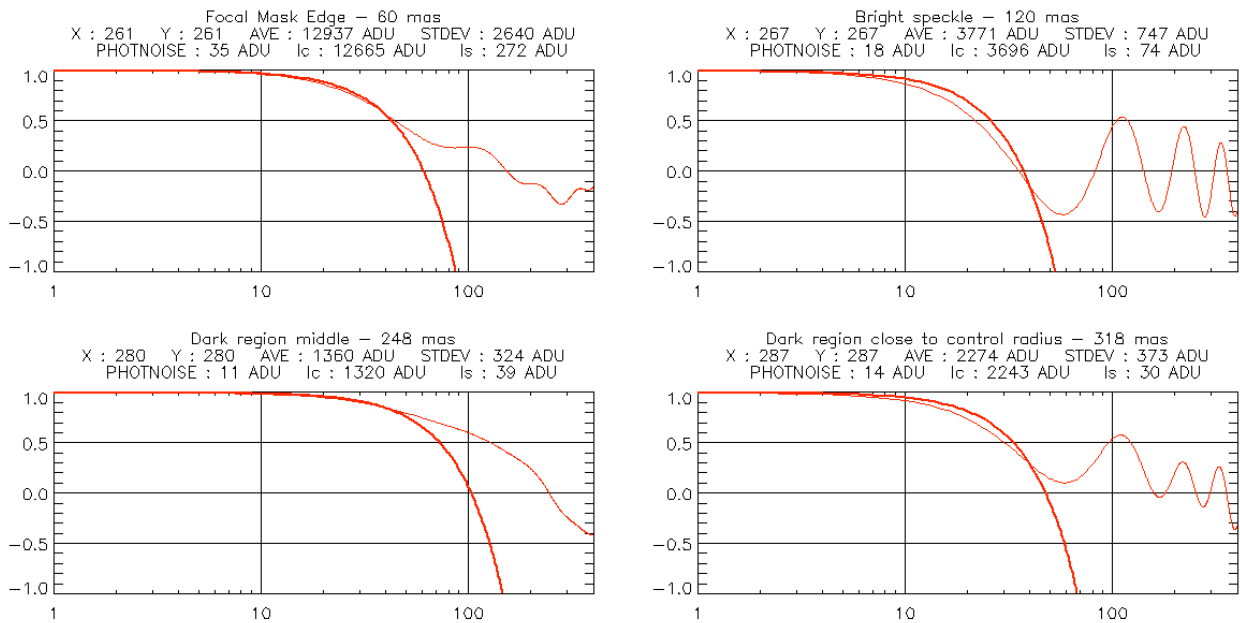


Figure 10 Single Difference autocorrelation of quasi-static part of four selected pixels of SD00 (red). Only a fit (thick red curve) to the first part of the curve that applies to high auto correlation has been made for SD00. The x-axis is shown on a logarithmic scale just for the purpose of showing the autocorrelation behaviour at short time more clearly.

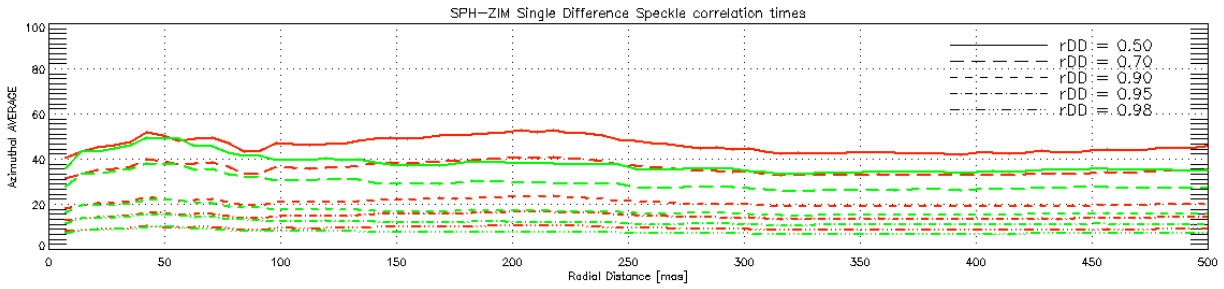


Figure 11 Single Difference correlation times (top panel) SD00 (left) and SD45 (right) to achieve an autocorrelation of 0.5 (bottom panel) azimuthal average profiles for auto-correlations of 0.50, 0.70, 0.90, 0.95 and 0.98 to achieve a DD performance increase of 1.4, 1.8, 3.2, 4.5 and 7.1 respectively. The HWP2 must switch on a timescale of about half the correlation time.

For our alpha Gru observations we have switched HWP2 after about 60 seconds. We have calculated the cross-correlation between the SD00 and SD45 frames. The resulting DD cross-correlation frame and azimuthal profile are shown in Figure 12. We conclude that the two SD frames are un-correlated. Therefore we can only gain a factor  $\sqrt{2}/2 = 1/\sqrt{2}$  from the DD frame combination. We conclude that the DD gain in our observations is not better than for two random SD datasets.

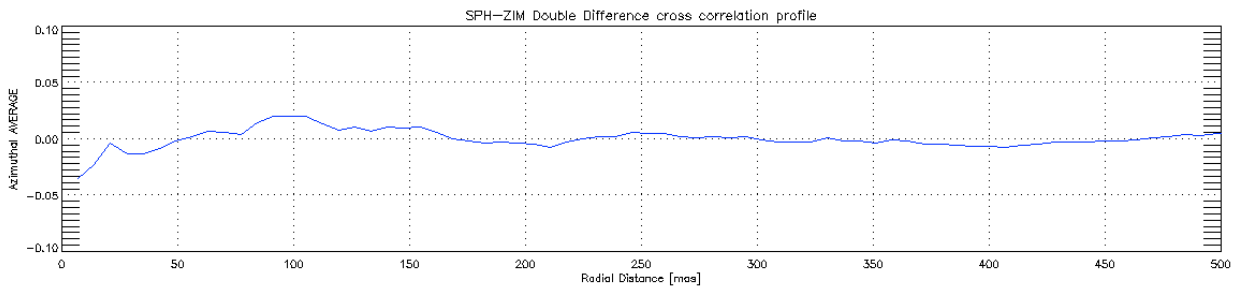
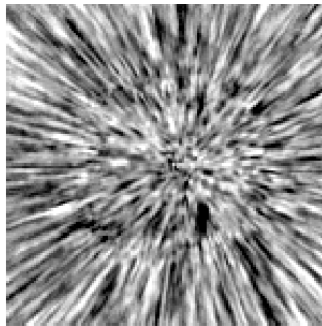


Figure 12 Double Difference cross correlation image (top panel) and azimuthal profile (bottom panel)

## Polarized background

The polarization measured at the ZIMPOL detectors is a combination of polarization introduced before (M1, M2, M3, HWP1 and M4) and after HWP2 (the SPHERE optical components and in particular the derotator). The HWP2 switch allows disentangling these two contributions according to

$$\text{Before HWP2:} \quad DD\_min = (SD00 - SD45)/2$$

$$\text{After HWP2:} \quad DD\_plus = (SD00 + SD45)/2$$

To avoid detector cross talks the instrumental polarization must be limited to smaller than 1%. We verify the instrumental polarization introduced before and after HWP2. The sign of the polarization before HWP2 will change sign upon a HWP2 switch of 45 degrees whereas the sign of the polarization introduced after HWP2 will stay the same. This allows to disentangle the polarization contributions before and after HWP2 by subtracting or adding the single difference frames. The results are shown in Figure 13. In the range of 100-200 mas we observe an instrumental polarization introduced after HWP2 of about 0.5% and an instrumental polarization introduced before HWP2 of about 0.9%. The instrumental polarization after HWP2 is strongly reduced by the Polarization Compensator. In principle the polarization before HWP2 is kept constant by the tracking of HPW1. We also observe strong polarization features between the edge of the coronagraph focal mask at 50 mas and about 100 mas that are probably introduced by beamshift effects. However, we can conclude that outwards of about 100 mas we are able to keep the polarization level < 1%.

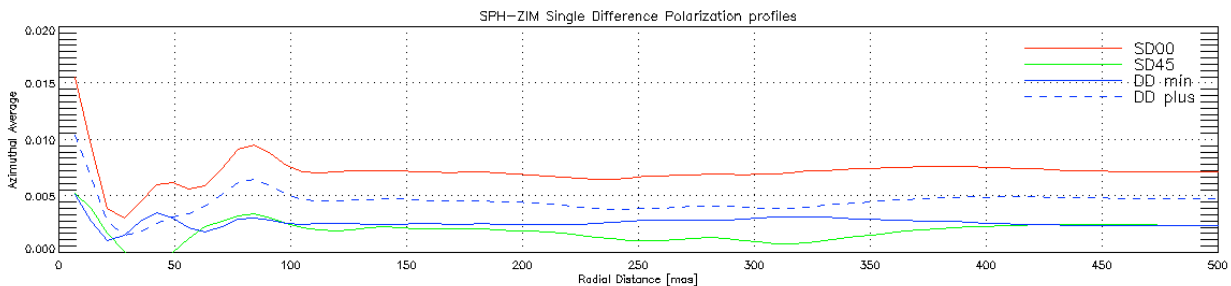


Figure 13 (top panel) Double Difference noise (top panel) Polarized speckle pattern before HWP2 (left) and after HWP2 (right) (bottom panel) azimuthal average (normalized) polarization profiles.

The polarized speckle pattern after HWP2 is subtracted in the regular applied DD\_min. However, we see that we have a noisy polarized speckle pattern introduced before HWP2 that can't be removed by the Double Difference in regular PDI data processing. We conclude that a fixed polarized speckle pattern introduced before HWP2 will dominate the PDI noise performance.

## 4. NOISE REDUCTION

In this section we quantify the noise reduction in the DD frames from the following subsequent steps:

1. Polarimetric Differential Imaging (PDI)
2. PDI and Angular Differential Imaging (ADI<sup>[15]</sup>)
3. PDI, ADI and Average Frame subtraction

### 4.1 PDI

We apply classical PDI data-reduction without any field derotation. Clearly such data processing will never reveal any polarized planets. However, the reduced data serves as a reference to quantify the performance improvement when we apply field derotation and average frame subtraction. The results are shown in Figure 14.

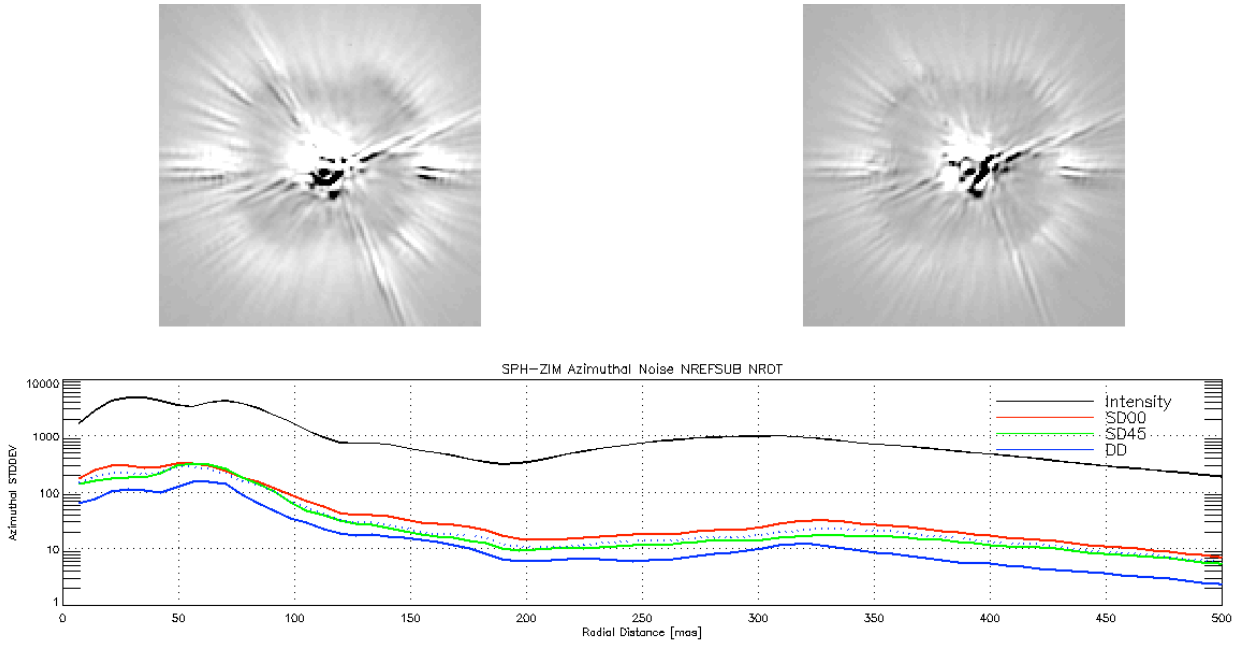


Figure 14 PDI noise (top panel) Polarized speckle patterns for SD00 (left) and DD (right) images (bottom panel) azimuthal standard deviation for intensity (black), SD00 (red), SD45 (green) and DD (blue)

### 4.2 PDI and ADI

Before we apply classical PDI data reduction we de-rotate the frames to account for the natural field rotation. We estimate the number of independent speckle pattern realizations  $M$  as function of radial distance  $r_{mas}$  in marcsec

$$M = 0.001 \times \alpha \times r_{mas}$$

where  $\alpha$  is the field rotation angle during the observation. If we assume that the speckle patterns are independent we expect a noise reduction of  $1/\sqrt{M}$ . For our Alpha Gru observation we have realized a field rotation of 23.5 degrees and hence we expect a noise reduction of a factor of 2.2 at 200 marcsec. Figure 15 shows the PDI and ADI results.

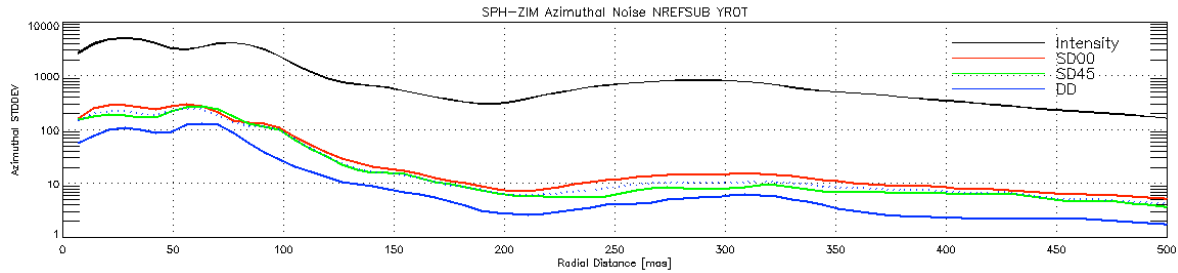


Figure 15 PDI and ADI noise (top panel) Polarized speckle patterns for SD00 (left) and DD (right) images (bottom panel) azimuthal standard deviation for intensity (black), SD00 (red), SD45 (green) and DD (blue)

### 4.3 PDI, ADI and Average Frame subtraction

We concluded a strong polarized speckle pattern that was introduced before HWP2 that doesn't subtract in the Double Difference. However, given the fact that SPHERE is designed for very high stability we expect this pattern to be both very stable and to be locked to the instrument even if we don't observe in pupil stabilized mode. Therefore we expect a significant gain in performance if we subtract the average frame of each each datasets DATA\_00\_UP, DATA\_00\_DN, DATA\_45\_UP and DATA\_45\_DN from each individual frame before we apply field de-rotation and frame combination. We verify this assumption by calculating the 2D-cross correlation of each individual frame with the average frame (see figure Figure 16). From the figure we see a correlation better than 0.98 and therefore we expect a gain in performance of about  $1/\sqrt{1-0.98} \sim 7$ . However, the average frame subtraction will come at the penalty of a reduction of the planet signal that we estimate as  $(M-1)/M$ , i.e. about a factor of 0.75-0.80 for our alpha Gru observation.

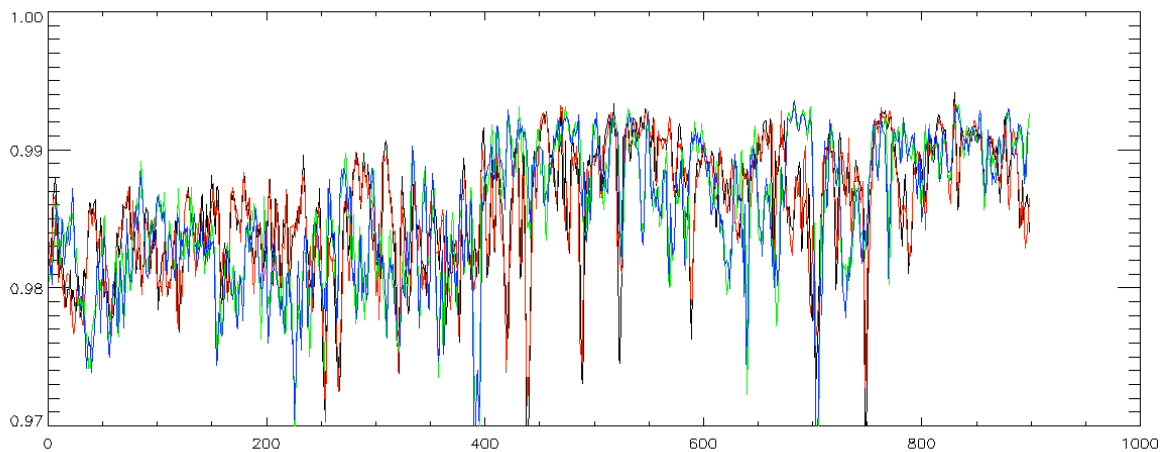


Figure 16 Cross-correlation between average frame and individual frames. DATA\_00\_UP (black), DATA\_00\_DN (red), DATA\_45\_UP (green) and DATA\_45\_DN (blue)

Figure 17 shows the results if we apply the PDI, AID and Average Frame subtraction.

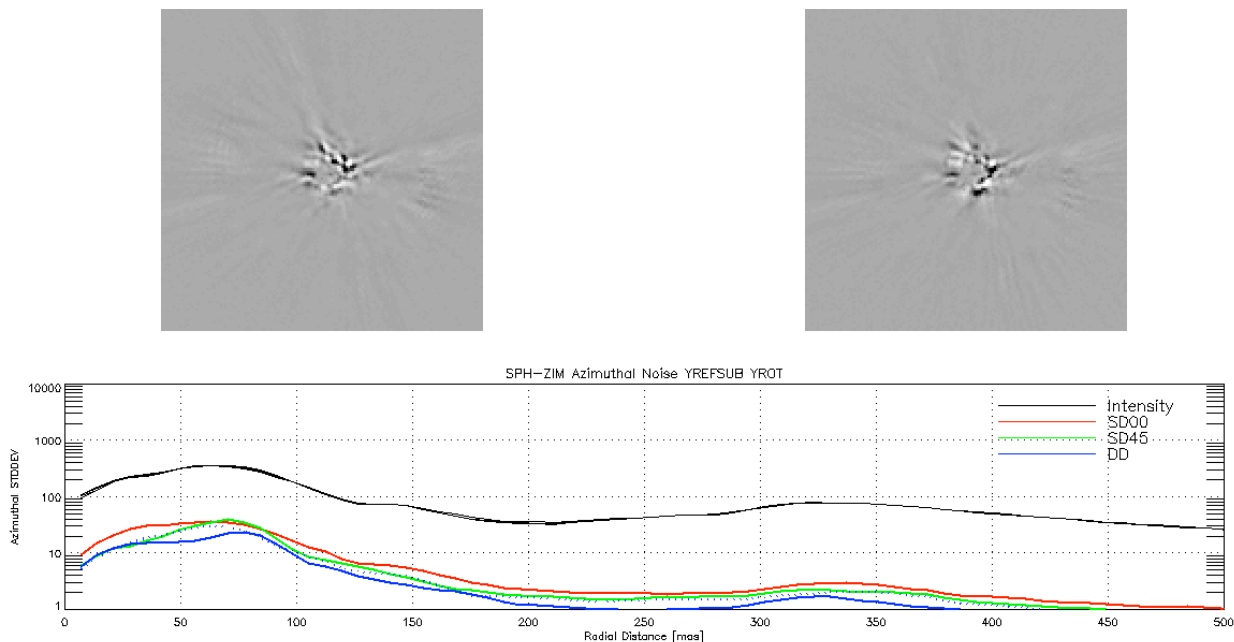


Figure 17 PDI, ADI and Average Frame subtraction noise (top panel) Polarized speckle patterns for SD00 (left) and DD (right) images (bottom panel) azimuthal standard deviation for intensity (black), SD00 (red), SD45 (green) and DD (blue)

We will try to compare the gain in noise reduction that we have achieved with our predictions. Figure 18 shows the achieved gains by image rotation and average frame subtraction as well as the predictions. We see that within 220 mas the prediction for the image rotation matches quite well with the predicted gain. For the average frame subtraction we expected a gain of about a factor of 7. We see that the gain in the region between 80 and 220 mas the gain is only about a factor of 3. However, the real benefit of the average frame subtraction seems to be close to the PSF core where we actually gain a factor of 7 in noise reduction. Probably the average frame subtraction provides a calibration of beamshift effects that are most prominent close to the PSF core.

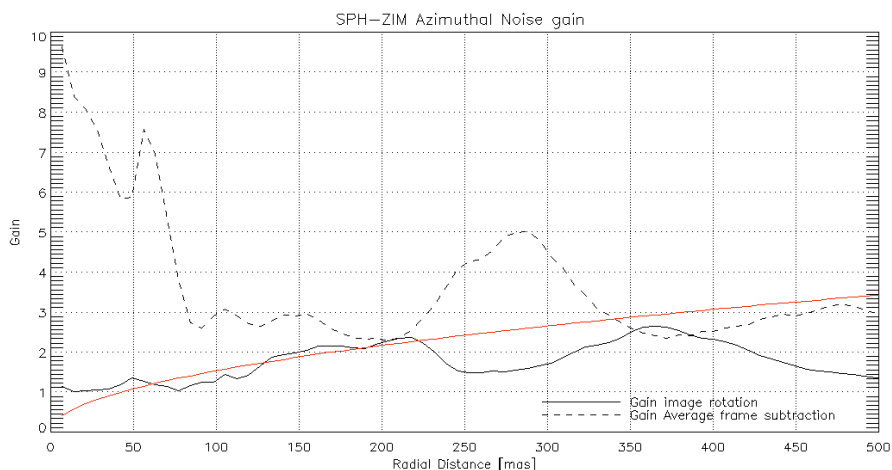


Figure 18 Azimuthal noise gain for image rotation (solid black) and average frame subtraction (dash black). Prediction for gain by image rotation (solid red), for average frame subtraction we expected an overall gain of about a factor of 7.

## 5. CONCLUSION

We estimate the achieved contrast levels from the PDI, ADI and Average Frame subtracted DD frame. The bottom panel of Figure 19 shows the azimuthal average noise profiles, i.e. we have divided the azimuthal standard deviations with the non-coronagraphic PSF peak intensity level. We conclude that we achieve a contrast of  $10^{-7}$  between 200 and 300 mas where we are about a factor of 2.5 above the photon noise level at  $4e-8$ . However, bad regions in the image like the telescope or DM spiders can significantly affect the azimuthal average or standard curves.

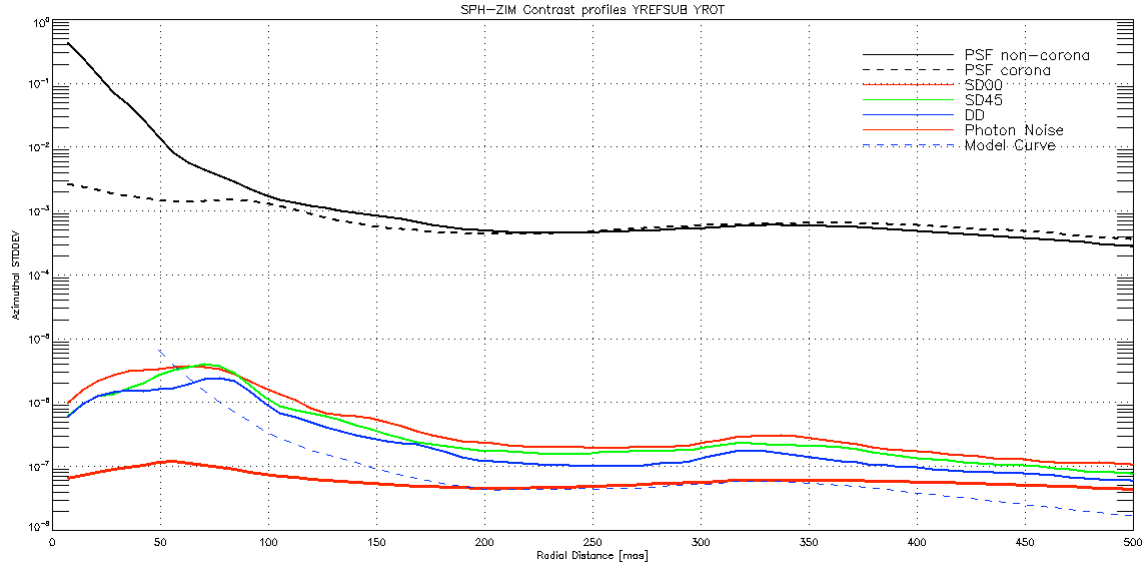


Figure 19 Contrast curves normalized to non-coronagraphic PSF peak intensity. From top to bottom: non-coronagraphic intensity, coronagraphic intensity, SD00 (red), SD45 (green), DD (blue) and Photon Noise (thick red) profile.

Therefore in Figure 20 we construct a contrast plot of the image plane. From the DD frame for each pixel we have calculated the standard deviation for a box of the  $6 \times 6$  neighboring pixels. Subsequently we have divided these values by the non-coronagraphic PSF peak intensity. From the image we see that especially in the regions between 200 and 300 mas we have relatively large areas where we reach contrasts very close to the photon noise limit of  $4e-8$ .

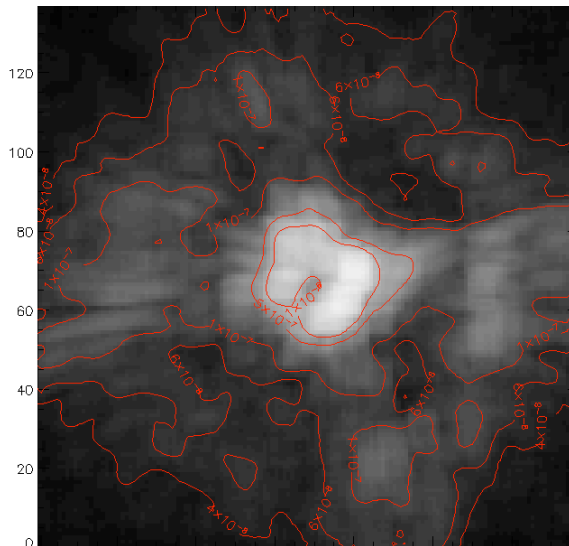


Figure 20 Contrast plot

Table 1 Estimated contrast levels for ZIMPOL prime targets for Jupiter sized planets with an albedo of 0.13 and a polarization of 0.20.

	Distance (parsec)	Angular Separation (arcsec)	Angular Separation (arcsec)	Angular Separation (arcsec)	Angular Separation (arcsec)
		0.05	0.1	0.2	0.25
a Cen A	1.34	1.3E-06	3.3E-07	8.3E-08	5.3E-08
a Cen B	1.34	1.3E-06	3.3E-07	8.3E-08	5.3E-08
Sirius A	2.67	3.3E-07	8.3E-08	2.1E-08	1.3E-08
Procyon	3.50	1.9E-07	4.8E-08	1.2E-08	7.7E-09
Altair	5.14	9.0E-08	2.2E-08	5.6E-09	3.6E-09
eps Eri	3.22	2.3E-07	5.7E-08	1.4E-08	9.1E-09
tau Cet	3.65	1.8E-07	4.4E-08	1.1E-08	7.1E-09
eps Ind	3.63	1.8E-07	4.5E-08	1.1E-08	7.2E-09

We can estimate the contrast for a Jupiter sized planet with albedo  $a$  and planet polarization  $p$  with a simple expression

$$C = (2.28 \times 10^{-7}) \frac{a \times p}{(\theta \times R_p)^2}$$

Here the angular distance  $\theta$  is in units of [asec] and the earth-star distance in units of [parsec]. The albedo and planet polarization are strongly dependent on the planet phase angle. Here we adopt the values  $a = 0.13$  and  $p = 0.20$  that roughly correspond to a phase angle of 80 degrees. Table 1 lists the expected contrast levels for the ZIMPOL prime targets for several angular separations.

From our alpha Gru data we conclude that from an instrumental point of view we have realistic prospects of detecting a polarized planet around a Cen A and B around 200 mas.

## REFERENCES

- [1] Schmid, H. M., Beuzit, J.-L., Feldt, M., Gisler, D., Gratton, R., Henning, T., Joos, F., Kasper, M., Lenzen, R., Mouillet, D., Moutou, C., Quirrenbach, A., Stam, D. M., Thalmann, C., Tinbergen, J., Verinaud, C., Waters, R., and Wolstencroft, R., "Search and investigation of extra-solar planets with polarimetry," IAU Colloq. 200, 165–170 (2006)
- [2] D. Gisler, H.M. Schmid, C. Thalmann, H.P. Povel, J.O. Stenflo, F. Joos, M. Feldt, R. Lenzen, J. Tinbergen, R. Gratton, R. Stuik, D.M. Stam, W. Brandner, S. Hippler, M. Turatto, R. Neuhauser, C. Dominik, A. Hatzes, Th. Henning, J. Lima, A. Quirrenbach, L.B.F.M. Waters, G. Wuchterl, H. Zinnecker, "CHEOPS/ZIMPOL: a VLT instrument study for the polarimetric search of scattered light from extrasolar planets," Proc. SPIE 5492, 463-474 (2004)
- [3] Beuzit, J.-L., Feldt, M., Dohlen, K., Mouillet, D., Puget, P., Antichi, J., Baruffolo, A., Baudoz, P., Berton, A., Boccaletti, A., Carbillet, M., Charton, J., Claudi, R., Downing, M., Feautrier, P., Fedrigo, E., Fusco, T., Gratton, R., Hubin, N., Kasper, M., Langlois, M., Moutou, C., Mugnier, L., Pragt, J., Rabou, P., Saisse, M., Schmid, H. M., Stadler, E., Turrato, M., Udry, S., Waters, R., and Wildi, F., "SPHERE: A 'Planet Finder' Instrument for the VLT," The Messenger 125, 29–34 (2006)
- [4] Jean-François Sauvage, Jean-Luc Beuzit, Ronald roelfsema, et al., "Sphere: complete laboratory performance and prediction for on-sky first light," Proc. SPIE 8864, 88640B (2013)
- [5] Kjetil Dohlen, Michel Saisse et al., "Manufacturing and integration of the IRDIS dual imaging camera and spectrograph for SPHERE," Proc. SPIE 7735, (2010)

- [6] Ricardo Claudi, "SPHERE IFS: The spectro differential imager of the VLT for exoplanets search," Proc. SPIE 7735, (2010)
- [7] C. Petit , J.-F. Sauvage , A. Sevin ; A. Costille , T. Fusco , P. Baudoz , J.-L. Beuzit , T. Buey , J. Charton , K. Dohlen , P. Feautrier , E. Fedrigo , J.-L. Gach , N. Hubin , E. Hugot , M. Kasper , D. Mouillet , D. Perret , P. Puget , J.-C. Siquin , C. Soenke , M. Suarez , F. Wildi, "The SPHERE XAO system SAXO: integration, test, and laboratory performance," Proc. SPIE 8447, (2012)
- [8] D. M. Stam, "Spectropolarimetric signatures of Earth-like extrasolar planets," A&A 482, 989-1007 (2008)
- [9] E. Buenzli, H.M. Schmid, "A grid of polarization models for Rayleigh scattering planetary atmospheres," Astron. Astrophys. 504, 259-276 (2009)
- [10] Povel, H. P., Aebersold, F., and Stenflo, J., "Charge-coupled device image sensor as a demodulator in a 2-D polarimeter with a piezoelectric modulator," Appl. Opt. 29, 1186 (1990)
- [11] Schmid, Hans-Martin; Downing, Mark; Roelfsema, Ronald; Bazzon, Andreas; Gisler, Daniel; Pragt, Johan; Cumani, Claudio; Salasnich, Bernardo; Pavlov, Alexey; Baruffolo, Andrea; Beuzit, Jean-Luc; Costille, Anne; Deiries, Sebastian; Dohlen, Kjetil; Dominik, Carsten; Elswijk, Eddy; Feldt, Markus; Kasper, Markus; Mouillet, David; Thalmann, Christian; Wildi, François, "Tests of the demodulating CCDs for the SPHERE / ZIMPOL imaging polarimeter," Proc. SPIE 8446, (2012)
- [12] Andreas Bazzon , Daniel Gisler , Ronald Roelfsema , Hans M. Schmid , Johan Pragt , Eddy Elswijk , Menno de Haan , Mark Downing , Bernardo Salasnich , Alexey Pavlov , Jean-Luc Beuzit , Kjetil Dohlen , David Mouillet , François Wildi, "SPHERE / ZIMPOL: characterization of the FLC polarization modulator," Proc. SPIE 8446, (2012)
- [13] Ronald Roelfsema , Daniel Gisler , Johan Pragt , Hans Martin Schmid , Andreas Bazzon , Carsten Dominik , Andrea Baruffolo , Jean-Luc Beuzit , Julien Charton , Kjetil Dohlen , Mark Downing , Eddy Elswijk , Markus Feldt , Menno de Haan , Norbert Hubin , Markus Kasper , Christoph Keller , Jean-Louis Lizon , David Mouillet , Alexey Pavlov , Pascal Puget , Sylvain Rochat , Bernardo Salasnich , Peter Steiner , Christian Thalmann , Rens Waters , François Wildi, "The ZIMPOL high contrast imaging polarimeter for SPHERE: sub-system test results," Proc. SPIE 8151, (2011)
- [14] Remi Soummer, The Astrophysical Journal 669, 642-656 (2007)
- [15] Marois, C., Lafrenière, D., Doyon, R., Macintosh, B., and Nadeau, D., "Angular Differential Imaging: A Powerful High-Contrast Imaging Technique," The Astrophysical Journal 641, 556–564 (2006)